Asian Journal of Current Research in Clinical Cancer
ISSN: 3062-4444
2022, Volume 2, Issue 1, Page No: 126-138

Available online at: www.galaxypub.co/page/journals

Galaxy Publication

Galaxy Publication

Voxel-Wise Analysis of Infratentorial Brain Metastases Reveals Associations with Clinical Features and Outcomes

S.K. Lim[1*], C.H. Tan[1], E. Wong[1]

[1]Department of Cancer Therapy, School of Medicine, National University of Singapore, Singapore.

***E-mail** ✉ cancer.therapy.nus.16@emailprovider.net

Received: 11 March 2022; **Revised:** 29 May 2022; **Accepted:** 03 June 2022

ABSTRACT

Brain metastases (BMs) frequently involve infratentorial regions, yet the clinical implications of metastases in these areas remain unclear. In this retrospective analysis, 1102 patients with a total of 4365 BM lesions were examined. MRI scans were processed using voxel-wise mapping to create normalized tumor frequency heatmaps, and Analysis of Differential Involvement (ADIFFI) identified clusters with statistical significance. Survival outcomes were evaluated using Kaplan-Meier analysis and Cox proportional hazards models. High relative risk of metastasis was observed in the parietal, insular, left occipital lobes, and cerebellum. Site-specific patterns were evident, with lung, breast, and colorectal cancer BMs frequently affecting infratentorial regions, while melanoma BMs were less common in these locations. Significant infratentorial clusters were associated with younger patients, male sex, lung neuroendocrine and squamous cell carcinomas, elevated Ki-67 expression, and poorer clinical outcomes. Patients with three or more BMs and those receiving whole-brain radiotherapy alone had worse overall survival. In patients undergoing surgical treatment, infratentorial BM involvement was an independent predictor of poor prognosis ($p = 0.023$; hazard ratio = 1.473; 95% CI: 1.055–2.058). These results improve understanding of BM spatial patterns and offer guidance for diagnosis, treatment strategies, and prognostic evaluation.

Keywords: Brain metastases, MRI, Infratentorial, Prognosis, Voxel-wise mapping

How to Cite This Article: Lim SK, Tan CH, Wong E. Voxel-Wise Analysis of Infratentorial Brain Metastases Reveals Associations with Clinical Features and Outcomes. Asian J Curr Res Clin Cancer. 2022;2(1):126-38. https://doi.org/10.51847/tjwUuUDzCF

Introduction

Brain metastases (BMs) are a leading cause of cancer-related death, occurring far more frequently than primary brain tumors—up to ten times higher in incidence. Estimates suggest that 7–14 individuals per 100,000, or 10–30% of systemic cancer patients, develop BMs [1–3]. The presence of multiple metastatic lesions in nearly 40% of patients, combined with the limited permeability of the blood-brain barrier to systemic chemotherapies, renders BMs particularly challenging to treat and contributes to a poor prognosis [4]. In addition to systemic therapy, local interventions—including surgical resection, whole-brain radiotherapy (WBRT), and stereotactic radiosurgery (SRS)—remain essential components of BM management [5].

Effective treatment planning requires consideration of tumor-specific characteristics such as lesion number, size, anatomical location, and the extent of surrounding edema [6]. Among these, the spatial distribution of BMs significantly influences both symptomatology and therapeutic strategies and has been linked to patient outcomes [7, 8]. Magnetic resonance imaging (MRI) enables precise mapping of metastases, and voxel-based analyses of these images have revealed patterns associated with primary tumor types. Previous studies identified a predilection for metastases to occur at the grey-white matter junction and watershed regions, attributed to tumor emboli lodging in distal arterial territories [9–11]. More recent voxel-wise mapping highlighted the posterior fossa as a frequent metastatic site for lung and breast cancer BMs, whereas melanoma metastases appear to rarely involve this region [10, 12–16]. Such observations have implications for early detection, differential diagnosis, and prophylactic strategies such as cranial irradiation.

Despite these findings, the infratentorial regions are affected unevenly depending on the origin of the primary tumor. Previous descriptive voxel-based studies provide limited statistical assessment, leaving the relationship between infratentorial BM localization and other clinical factors unclear. Additionally, the prognostic relevance of infratentorial involvement remains uncertain. To address this gap, we conducted a retrospective analysis of 1102 patients, examining how infratentorial BM distribution correlates with clinical features—including age, sex, primary tumor type, Ki-67 index, and overall survival—using voxel-wise mapping and multivariable analyses to determine potential independent prognostic indicators.

Results and Discussion

Patient characteristics and MRI workflow

A total of 1102 patients met the inclusion criteria. Patients were identified either through histopathological confirmation of brain lesions combined with MRI (n = 222) or through histopathology of primary tumors with radiological evidence of brain metastases (n = 880). The cohort included 667 males and 435 females, with a mean age of 59.8 years **(Figure 1a)**. The most common primary cancers were lung (86.1%), breast (4.2%), colorectal (2.5%), head and neck (1.3%), kidney (1.1%), and melanoma (0.6%), with other malignancies comprising 4.2%. Among 991 patients with follow-up data, median overall survival was 10.84 months. Treatment details were available for 402 patients, revealing that 48.3% underwent WBRT alone, while 36.3% had surgery only. Patient demographics and clinical characteristics are summarized in **Table 1**.

MRI data were processed through a series of steps including format conversion, spatial normalization, and semi-automated segmentation to delineate regions of interest (ROIs). These ROIs served as the foundation for the voxel-wise mapping analyses **(Figure 1b)**.

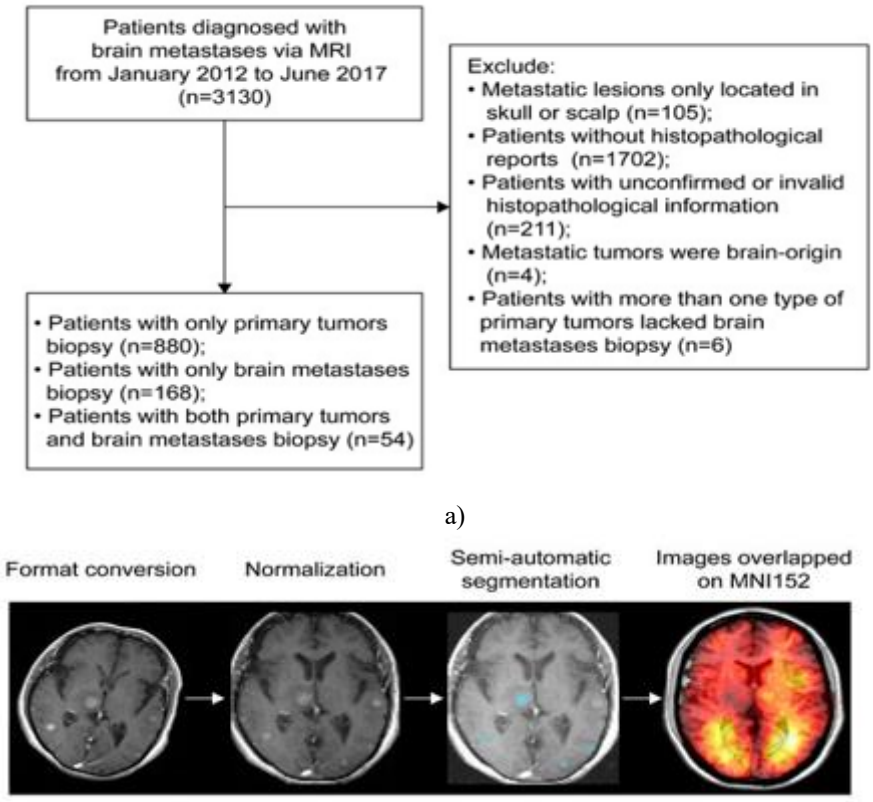

Figure 1. Patients inclusion and MRI data processing. (a) The workflow of inclusion and exclusion of brain metastases (BMs) patients. (b) Schematics of MRI data processing. The blue areas represent the regions of interest. MNI152 refers to the Montreal Neurological Institute 152 brain template and coordinate system. MRI refers to magnetic resonance imaging.

Table 1. Demographics.

Parameter	Category	Number (%)
Age at diagnosis (years)	Range	16–89
	Average	59.8
Sex	Male	667 (60.5)
	Female	435 (39.5)
Primary malignancies	Lung cancer	949 (86.1)
	Adenocarcinoma	630 (66.4)
	Squamous cell carcinoma	106 (11.2)
	Small cell lung cancer	169 (17.8)
	Other neuroendocrine subtypes	11 (1.1)
	Mesenchymal neoplasms	2 (0.2)
	Others	31 (3.3)
	Breast cancer	46 (4.2)
	Melanoma	7 (0.6)
	Kidney cancer	12 (1.1)
	Colorectal cancer	27 (2.5)
	Head and neck cancer	15 (1.3)
	Other cancer	46 (4.2)
Brain metastases number	N = 1	544 (49.4)
	N = 2	188 (17.0)
	N ≥ 3	370 (33.6)
Overall survival for 991 patients (months)	Range	0.10–85.55
	Median survival	10.84
	95% Confidence Interval	9.768–11.915
Treatments Parameter	Surgery alone	146 (36.3)
	Whole-brain radiotherapy alone	194 (48.3)
	Stereotactic radiosurgery alone	10 (2.5)
	Surgery + whole-brain radiotherapy	37 (9.2)
	Surgery + stereotactic radiosurgery	15 (3.7)

Lesion count, volume, and relative metastatic risk of brain metastases

In total, 4,365 brain metastases were delineated using semi-automated segmentation. Among the patient cohort, 49.4% presented with a single metastasis, 17.0% had two lesions, and 33.6% had three or more **(Table 1)**. Lung cancer, particularly lung adenocarcinoma, was responsible for the majority of metastatic lesions **(Figure 2a)**.

We analyzed the number of metastases, total lesion volume (TV), and the volume of individual lesions (VSL) across different brain regions and primary tumor types. The frontal lobe harbored the greatest mean number of metastases, whereas the insular lobe exhibited relatively higher TV and VSL. Although differences in lesion counts between primary cancers were not statistically significant, the TV of metastases originating from lung cancer was comparatively smaller. In contrast, metastases from kidney and colorectal cancers, as well as melanoma, demonstrated larger individual lesion volumes.

Further stratification of lung cancer subtypes—including adenocarcinoma, squamous cell carcinoma, and small cell lung cancer—revealed that metastases from squamous cell carcinoma tended to have larger VSLs, despite occurring less frequently than those from adenocarcinoma or small cell carcinoma.

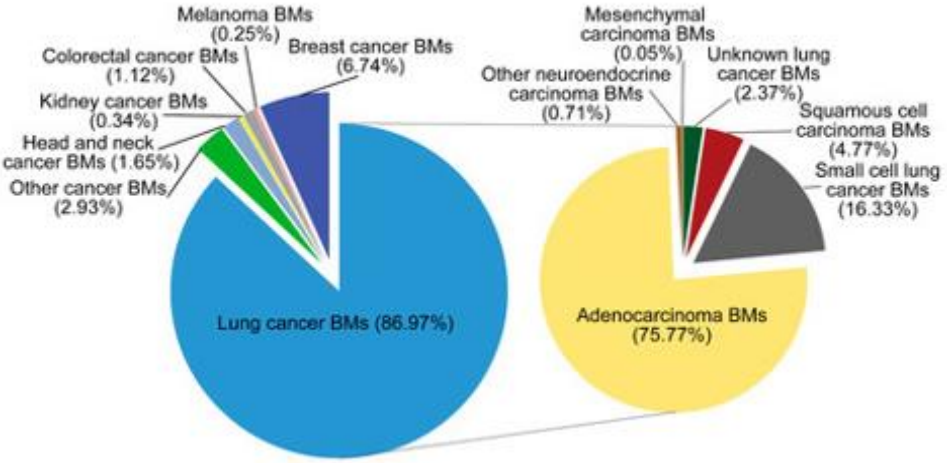

a)

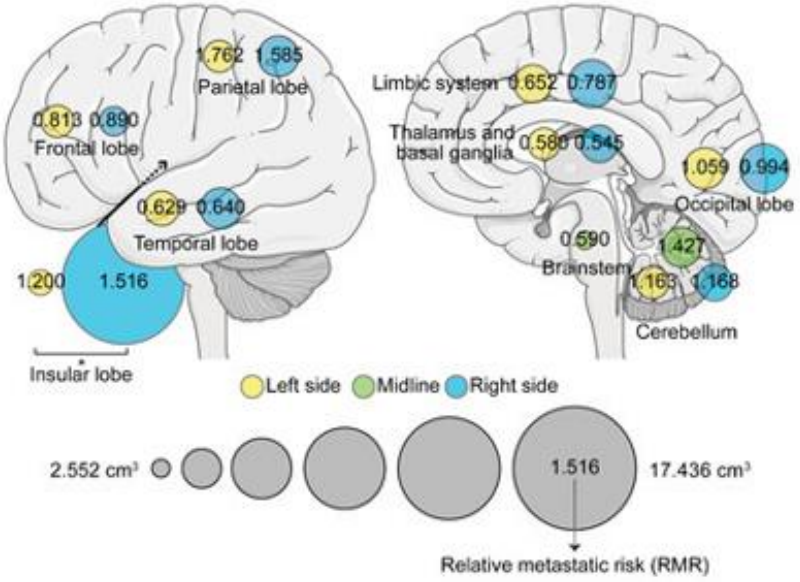

b)

Figure 2. Quantification and Regional Risk of Brain Metastases (BMs). (a) Pie charts illustrating the proportion of BMs originating from different primary tumor types. The right panel shows the distribution of BMs across lung cancer subtypes. (b) Diagram depicting the mean single-lesion volume across brain lobes and hemispheres (circle size), together with the relative metastatic risk (RMR), normalized to the volume of each lobe. *: $p < 0.05$.

Analysis of hemispheric differences indicated that lesions in the right insular lobe had a significantly greater volume compared to those on the left **(Figure 2b)**. To quantify regional susceptibility, the relative metastatic risk (RMR) was calculated by adjusting the observed BM counts to the volume of each corresponding brain region. Areas with RMR exceeding 1, indicating higher-than-expected BM occurrence, included the parietal, insular, left occipital lobes, and cerebellum. In contrast, the frontal lobe, temporal lobe, right occipital lobe, limbic structures, thalamus, basal ganglia, and brainstem exhibited lower-than-expected BM involvement (RMR < 1) **(Figure 2b)**.

Distribution of brain metastases by primary tumor

The spatial localization of 4,365 BM centroids was mapped according to primary tumor type. Infratentorial regions were consistently among the frequently affected sites. Tumor frequency heatmaps were generated by overlapping segmented ROIs **(Figure 1b)**, highlighting prominent clustering of BMs within the frontal, parietal,

occipital lobes, and posterior fossa **(Figure 3)**. Consistent with prior observations, metastases predominantly occurred at grey-white matter junctions and watershed areas, with a mild predilection for the left hemisphere. Stratification by tumor origin revealed distinct patterns: lung cancer metastases largely reflected the overall distribution due to their high prevalence. Breast cancer BMs localized mainly in the right cerebellum, while melanoma metastases were predominantly supratentorial. Colorectal cancer BMs preferentially involved the cerebellar vermis, kidney cancer lesions concentrated in the left frontal lobe, head and neck cancer metastases appeared in bilateral frontal lobes, and metastases from other malignancies were often infratentorial **(Figure 3)**.

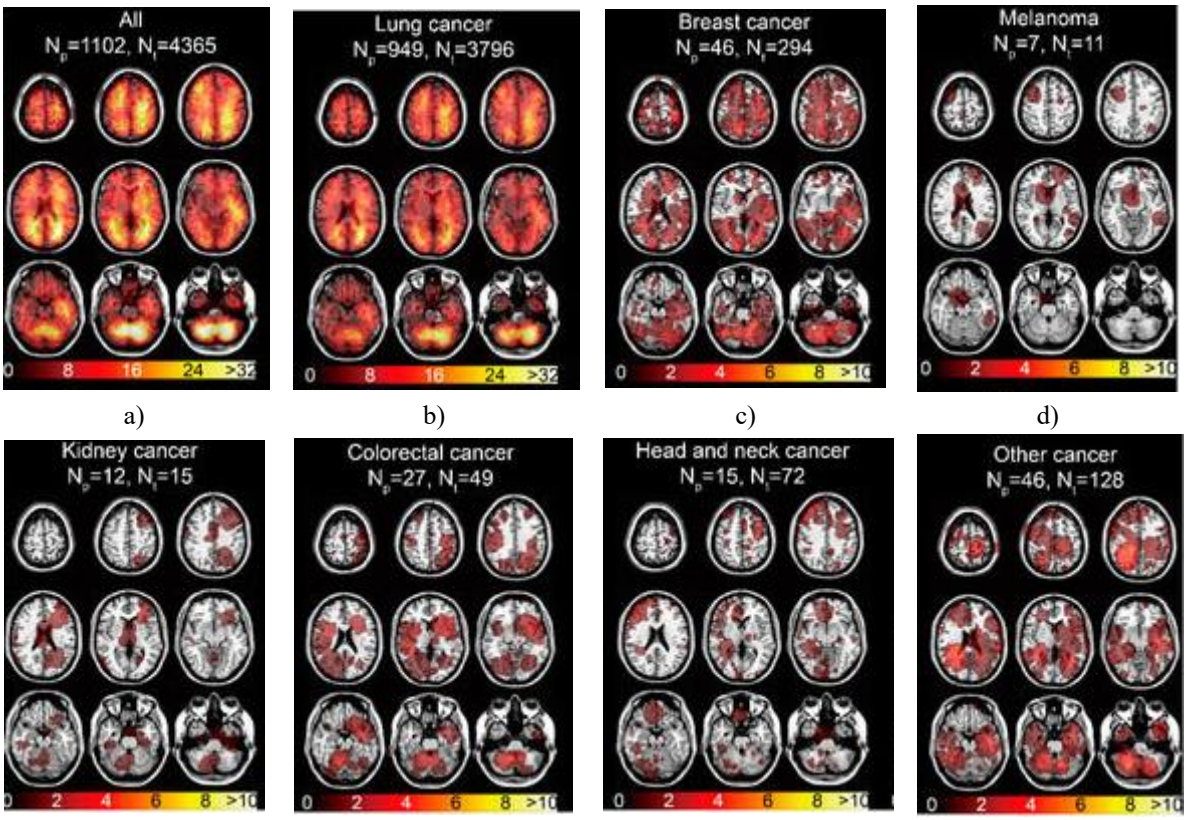

Figure 3. Brain Metastasis Frequency Maps by Primary Tumor Type. The color scale indicates the number of lesions, with Np denoting patient count and Nt the total tumor count.

Associations between infratentorial metastases and clinical features using ADIFFI

We applied the analysis of differential involvement (ADIFFI) to generate p-value heatmaps that quantify voxel-level associations with clinical characteristics [15, 16]. Age-stratified analysis (median 60.5 years) showed that older patients tended to have metastases concentrated in supratentorial regions, while younger patients exhibited greater involvement of infratentorial areas and the left frontal lobe (Fisher's exact test, $p < 0.05$; **(Figure 4a)**). Sex-specific patterns also emerged: female patients primarily had lesions near the parafalx, whereas male patients showed higher frequencies in the right frontal lobe, left parietal lobe, and left cerebellum **(Figure 4b)**.

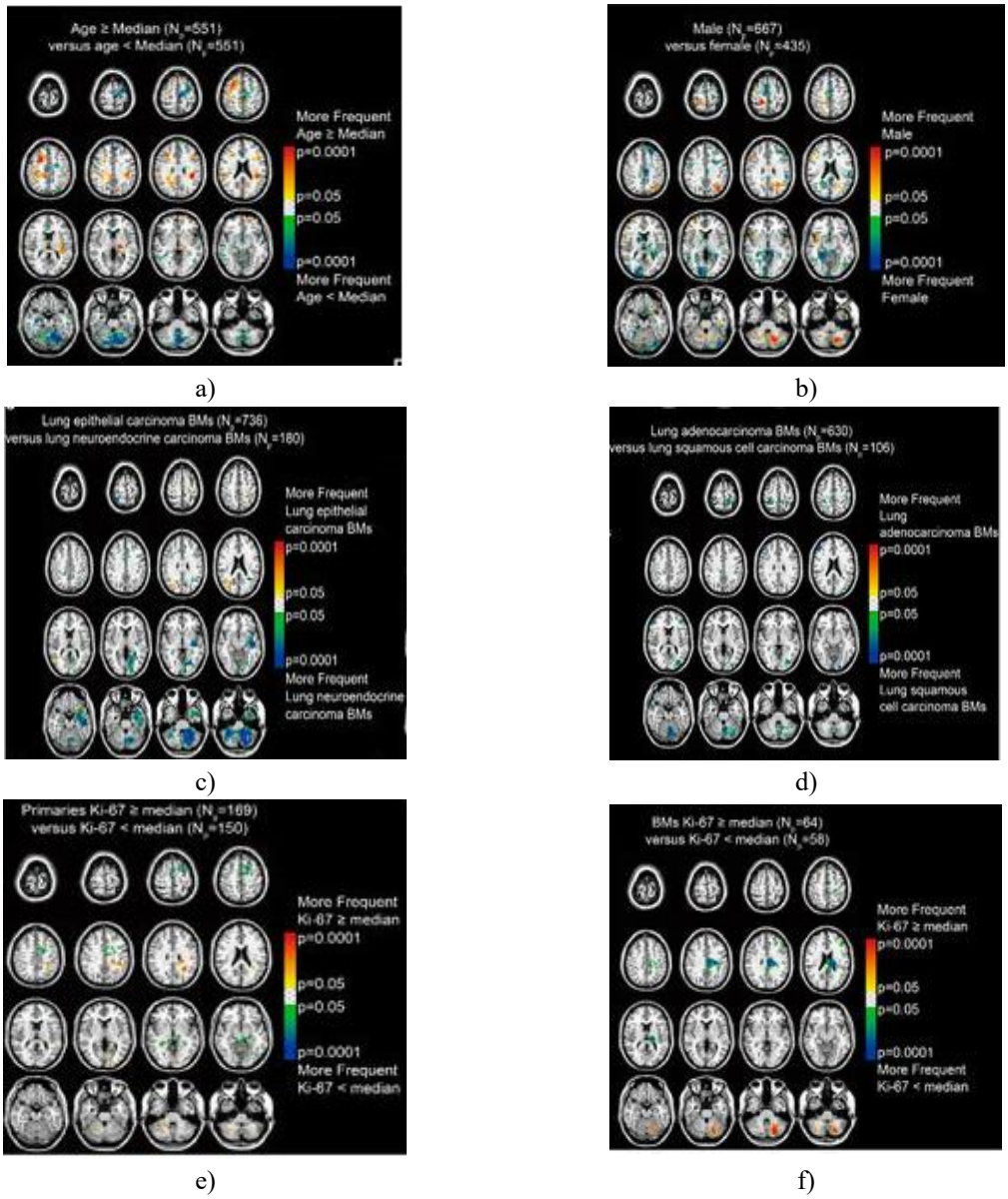

Figure 4. Differential involvement (ADIFFI) heatmaps highlighting regional BM patterns. Panels show voxel-wise comparisons: (a) patients above vs. below the median age (60.5 years), (b) male vs. female patients, (c) lung epithelial carcinoma vs. lung neuroendocrine carcinoma BMs, (d) lung adenocarcinoma vs. squamous cell carcinoma BMs, (e) primary tumors with Ki-67 ≥ median (35%) vs. < median, and (f) BMs with Ki-67 ≥ median (45%) vs. < median. Np indicates the number of patients.

Subgroup analysis by lung cancer type revealed distinct metastatic distributions. BMs originating from epithelial lung tumors primarily affected the right parietal and occipital lobes. In contrast, neuroendocrine lung carcinoma BMs were more commonly found in the left temporal lobe and infratentorial regions, particularly the left cerebellum **(Figure 4c)**. Among the epithelial carcinoma subtypes, squamous cell carcinoma metastases showed a preference for cortical and cerebellar regions compared to adenocarcinoma **(Figure 4d)**.

Proliferative index, reflected by Ki-67, was also associated with site-specific BM patterns. Patients with primary tumors exhibiting Ki-67 expression above the median (35%) had higher BM density in the left parietal and occipital lobes and infratentorial areas **(Figure 4e)**. Similarly, BMs with Ki-67 ≥ 45% were predominantly localized in the left cerebellum **(Figure 4f)**.

Infratentorial BMs and survival outcomes

Among 991 patients with follow-up data, the median overall survival was 10.84 months. Advanced age (≥ 60.71 years) and male sex were significantly associated with shorter OS ($p < 0.001$). Although patients with melanoma

BMs tended to have lower survival than those with other primaries, the difference did not reach statistical significance (p = 0.0945; **(Figure 5a)**). Lung cancer subtypes further stratified survival: patients with epithelial carcinoma BMs had better outcomes than those with neuroendocrine carcinoma BMs (p < 0.001). Within epithelial subtypes, adenocarcinoma BMs conferred a survival advantage compared to squamous cell carcinoma and small cell carcinoma BMs (p < 0.001). High Ki-67 expression was linked to poorer prognosis, both in primary tumors (≥ 35%, p = 0.0183) and in BMs (≥ 45%, p = 0.0484).

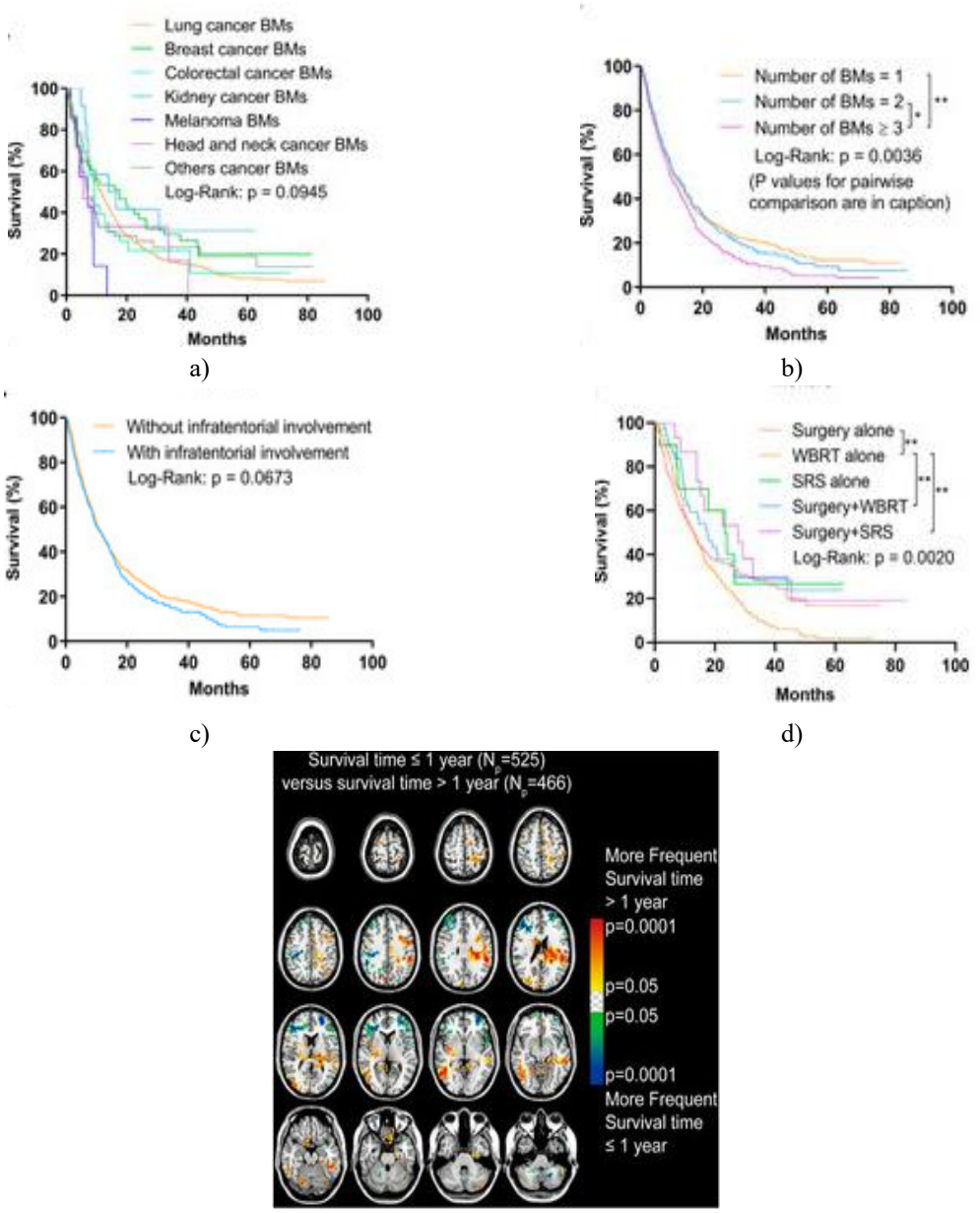

Figure 5. Overall survival (OS) analyses and ADIFFI of survival-associated BM locations. Panel (a) shows OS comparisons among patients with BMs originating from various primary cancers. Panel (b) presents OS stratified by BM count (1 vs. 2, p = 0.605; 1 vs. ≥3, p = 0.0010; 2 vs. ≥3, p = 0.0347). Panel (c) depicts OS differences between patients with and without infratentorial BMs. Panel (d) compares OS according to treatment received (surgery alone vs. WBRT alone, p = 0.005; surgery + WBRT vs. WBRT alone, p = 0.006; surgery + SRS vs. WBRT alone, p = 0.005). Panel (e) shows the ADIFFI-generated p-value heatmap highlighting BM clusters associated with OS ≤1 year versus >1 year. Np denotes patient numbers; WBRT, whole-brain radiotherapy; SRS, stereotactic radiosurgery; *p < 0.05, **p < 0.01.

Patients harboring three or more BMs exhibited significantly poorer OS compared to those with one or two lesions (p = 0.0036, **(Figure 5b)**). While OS differences between patients with or without infratentorial involvement were not statistically significant, a trend toward worse prognosis emerged in patients with infratentorial BMs after roughly one year of follow-up (p = 0.0673, **(Figure 5c)**).

Treatment modality was also strongly associated with survival. Patients who received WBRT alone had markedly shorter OS than those treated with surgery, surgery combined with WBRT, or surgery combined with SRS (p = 0.0020, **(Figure 5d)**).

Voxel-wise ADIFFI analysis further revealed survival-related BM patterns. Patients surviving longer than one year displayed significant clusters in the left frontal and parietal lobes and right occipital lobe, whereas those with OS ≤1 year had prominent clusters in the bilateral frontal lobes and cerebellum **(Figure 5e)**.

Infratentorial BMs as an independent prognostic risk factor in surgical patients

Surgical intervention remains a primary therapeutic strategy for patients with solitary BMs and is occasionally indicated for selected cases with multiple or recurrent lesions. To examine risk factors affecting prognosis in surgical patients, we analyzed 200 individuals who underwent resection. The Cox proportional hazards model evaluated age, sex, primary tumor type (lung, breast, or others), BM number, total tumor volume, location, and prior radiotherapy **(Table 2)**. Multivariate analysis demonstrated that infratentorial BM involvement independently predicted worse survival following surgery (p = 0.023, hazard ratio = 1.473, 95% CI = 1.055–2.058). Consistent with this finding, ADIFFI analysis of the same cohort revealed significant infratentorial BM clusters among patients with survival ≤1 year.

Table 2. Cox proportional hazards regression for brain metastases patients who received surgery.

Factors	**Number**	**Univariate**		**Multivariate**	
		HR (95% CI)	**p Value**	**HR (95% CI)**	**p Value**
Age		Average			59.8
(Median = 59.1 years)		Male			667 (60.5)
Young	100	Ref	Ref	Ref	Ref
Old	100	0.883 (0.640–1.218)	0.449	0.892 (0.643–1.238)	0.496
Sex					
Female	78	Ref	Ref	Ref	Ref
Male	122	1.293 (0.928–1.802)	0.129	1.239 (0.857–1.790)	0.255
Primaries					
Lung cancer	138	Ref	Ref	Ref	Ref
Breast cancer	14	1.077 (0.576–2.015)	0.816	1.209 (0.610–2.398)	0.586
Other cancer	48	1.128 (0.772–1.650)	0.533	1.150 (0.776–1.705)	0.486
Number					
N = 1	161	Ref	Ref	Ref	Ref
N = 2	25	1.142 (0.710–1.835)	0.584	1.036 (0.633–1.697)	0.888
N ≥ 3	14	2.132 (1.198–3.793)	0.010 *	1.751 (0.944–3.245)	0.075
Total volume					
(Median = 27.67 cm^3)					
Small	100	Ref	Ref	Ref	Ref
Large	100	1.325 (0.961–1.828)	0.086	1.245 (0.897–1.728)	0.190
Locations					
Without infratentorial involvement	136	Ref	Ref	Ref	Ref

With infratentorial involvement	64	1.473 (1.055–2.058)	0.023 *	1.473 (1.055–2.058)	0.023 *
Radiotherapy [1]					
No	146	Ref	Ref	Ref	Ref
Yes	54	0.738 (0.512–1.064)	0.103	0.778 (0.535–1.129)	0.186

[1] Radiotherapy includes whole-brain radiotherapy and stereotactic radiosurgery. * p values with statistical significance. Ref refers to reference. HR refers to hazard ratio. CI refers to confidence interval.

This study explored the spatial distribution of brain metastases (BMs) using voxel-wise mapping and ADIFFI in a large patient cohort, revealing connections between infratentorial BM localization, specific clinical characteristics, and patient prognosis.

BMs display considerable heterogeneity in both biological behavior and molecular features due to their diverse tumor origins. Radiological patterns, including lesion distribution, reflect some of this heterogeneity and are critical for guiding local therapeutic strategies. Magnetic resonance imaging (MRI) is a highly sensitive tool for detecting BMs and allows both visual assessment and data-driven analyses. Voxel-wise analysis of MRI data is increasingly applied in brain research, including studies of stroke and amyloid pathology. This approach offers the advantage of registering individual scans to a standard brain template, such as MNI152, which ensures that voxel coordinates are comparable across scans regardless of MRI field strength. Previous work using voxel-wise methods has successfully mapped preferred locations of meningiomas, highlighting its potential utility in assessing heterogeneous BM localization.

Using this methodology, we identified preferential BM sites, including the cerebellum for metastases originating from lung and breast cancers. Prior studies have also shown site-specific patterns in BMs from various breast cancer subtypes. Similarly, mapping studies across multiple primary malignancies demonstrated that gastrointestinal cancer BMs often involve infratentorial regions, whereas melanoma and sarcoma metastases tend to avoid these areas. The current tumor frequency heatmaps are consistent with these observations. Analysis of relative metastatic risk further confirmed the susceptibility of the cerebellum to BMs. Infratentorial BMs from gastrointestinal cancers, particularly colorectal cancer, have been hypothesized to arise through retrograde spread via Batson's plexus. Conversely, melanoma's avoidance of the cerebellum may involve mechanisms independent of VEGF-mediated vascular pathways.

The clinical significance of infratentorial BMs is notable. Surgical management of these lesions often requires more aggressive strategies due to the risks of obstructive hydrocephalus, brainstem injury, or herniation at the foramen magnum. From a pathophysiological perspective, two primary hypotheses—the entrapment of tumor emboli along metastatic routes and the interaction between tumor "seed" and host "soil"—help explain BM formation. Additionally, regional differences in vascular density, hemodynamics, and oxygenation may underlie the contrasting patterns of supratentorial versus infratentorial BM development, with infratentorial lesions typically arising in areas of higher perfusion.

Based on these considerations, we investigated associations between BM localization and clinical characteristics using the voxel-wise ADIFFI approach, previously applied to glioblastoma to correlate tumor distribution with molecular and genetic alterations. Our analyses indicated that infratentorial BMs were more likely in younger, male patients, in metastases from lung neuroendocrine and squamous cell carcinomas, and in tumors with high Ki-67 expression in both primary and metastatic sites. These findings are clinically relevant; for example, prophylactic cranial irradiation (PCI) is commonly used in small cell lung cancer (SCLC), a high-risk neuroendocrine subtype. Although PCI efficacy varies by disease stage, our results support targeting infratentorial regions during prophylactic therapy. Infratentorial clusters were also observed in squamous cell lung cancer BMs, which are generally more aggressive than adenocarcinomas, suggesting a link between tumor aggressiveness and infratentorial vulnerability. Notably, clusters associated with poor survival were relatively smaller, likely reflecting the combined effects of more aggressive treatment in infratentorial regions, younger patient age, and the overall non-significant impact of infratentorial involvement on survival across the entire cohort.

Beyond the infratentorial region, we identified significant clusters in the bilateral frontal lobes associated with shorter survival. This may reflect two factors: first, unilateral frontal lesions may extend contralaterally, producing diffuse disease; second, bilateral frontal involvement may significantly impair neurocognitive function, exacerbating the clinical impact of BMs.

As observed, there was no statistically significant association between BM location and overall survival **(Figure 5c)**. Kancharla and colleagues noted in their review that the impact of BM location on clinical outcomes remains debated, largely due to variations and limitations across studies. One of the main challenges is defining the anatomical location. Precise mapping of brain lobes and lesions spanning multiple lobes can be achieved using MNI152 registration combined with centroid calculations. However, grouping patients based on different location categories—such as supratentorial versus infratentorial or eloquent versus non-eloquent areas—may influence outcome analyses. In our study, patients were categorized by the presence or absence of infratentorial involvement. Multivariate analysis indicated that, for surgically treated patients, infratentorial BMs represented an independent predictor of worse survival. Supporting this, Enders *et al*. reported poorer outcomes in NSCLC patients undergoing surgery when BMs involved infratentorial regions. Likewise, studies examining WBRT doses found that infratentorial or combined supratentorial-infratentorial involvement independently predicted mortality. Conversely, analyses comparing cerebellar versus supratentorial BMs in radiosurgery-treated patients did not show a significant prognostic impact, highlighting that the survival relevance of BM location may depend on cohort characteristics and the definitions used.

Voxel-wise analyses also revealed differences in BM volumes across brain regions and primary tumor types, underscoring BM heterogeneity. In contrast to infratentorial regions, the hippocampus exhibited a relatively low risk for BM formation, as reflected by the sparse involvement seen in **Figure 3**. This evidence underpins the rationale for hippocampal-avoidance WBRT (HA-WBRT), which can reduce unnecessary radiation exposure to the hippocampus and limit cognitive toxicity compared to conventional WBRT. Our cohort also showed that patients treated with WBRT alone had the poorest overall survival **(Figure 5d)**. Beyond potential neurocognitive side effects, WBRT alone is generally reserved for palliative care in patients with widespread BM. Additionally, patients receiving only WBRT had significantly higher BM counts (5.34 ± 0.52 vs. 1.56 ± 0.15, $p < 0.001$) compared to those receiving other treatments, contributing to poorer outcomes.

This study has several limitations. Previous reports indicate that the most common primary tumors giving rise to BMs include lung cancer (43.3%), melanoma (16.4%), breast cancer (15.7%), colorectal cancer (9.3%), and renal cell carcinoma (9.1%). In contrast, 86.1% of our cohort had lung cancer BMs, which may reflect both the single-center design and regional cancer epidemiology. Fabi *et al*. highlighted that, compared to lung cancer, BMs from other primaries tend to appear later after diagnosis (e.g., breast cancer: 46 months; colorectal cancer: 42 months; melanoma: 22 months). Globally, the incidence of certain cancers varies by region; for example, age-standardized rates for lung cancer in Eastern Asia are comparable to North America, but breast and skin cancer incidences are lower. Thus, both tumor biology and regional prevalence likely influenced the predominance of lung cancer BMs in our sample.

We took care to avoid overgeneralizing our results. For instance, ADIFFI comparisons were not performed for tumor types with very small sample sizes, and our tumor frequency analyses were descriptive. Future research should include multi-center cohorts to ensure broader representation. Other limitations include reliance on histological confirmation of primary tumors only, without universal verification of BM pathology, and lack of exploration of molecular mechanisms underlying infratentorial predilection. Previous studies have shown that certain mutations are enriched in infratentorial IDH-mutant astrocytomas and pediatric cerebellar high-grade gliomas, suggesting biological underpinnings that warrant experimental investigation. Finally, leptomeningeal metastases are known to worsen prognosis, but our voxel-wise segmentation approach could not capture leptomeningeal enhancement, highlighting the need for methodological improvements to evaluate their clinical impact.

Materials and Methods

Patient cohort

We retrospectively screened 3,130 patients who were initially diagnosed with brain metastases (BMs) using contrast-enhanced T1-weighted MRI (CE-T1WI) at our hospital between January 2012 and June 2017. Patients whose lesions were restricted to the skull or scalp (n = 105) were excluded. Histopathological data were retrieved for the remaining 3,025 patients, and 1,323 of these had complete records linking primary tumors and BMs. Inclusion criteria were: (1) biopsy-confirmed BMs, with or without a primary tumor biopsy, and (2) biopsy of only the primary tumor if BM sampling was contraindicated. Patients were excluded if histopathology was inconclusive, BMs originated from primary brain tumors, or multiple primaries were present without BM biopsy.

After rigorous review and MRI evaluation by a senior neuroradiologist (B.J.), 1,102 patients were included for analysis. The patient selection workflow is illustrated in **Figure 1a**. The dataset is available from the corresponding author upon request.

Ethical approval and patient consent

This study was conducted according to the Declaration of Helsinki. At hospital admission, all patients provided written consent permitting the use of their imaging, histopathological, and clinical data for research and educational purposes. Retrospective data collection and publication were approved by the Institutional Ethical Committee on Clinical Human Research (Approval No. 2020–801). Patient information was de-identified prior to analysis.

MRI acquisition

MRI scans were acquired using either a 1.5-Tesla (Signa Excite, GE Healthcare, Milwaukee, WI) or 3.0-Tesla system (Discovery 750, GE Healthcare, Milwaukee, WI). CE-T1WI was obtained following intravenous administration of gadodiamide (0.2 mL/kg, max 20 mL). The imaging protocol used turbo spin echo sequences with 6 mm section thickness. TR/TE values were 400–1,750 ms / 6.9–10 ms for 1.5T and 1,750–2,080 ms / 24.62–25.15 ms for 3T. For patients with multiple scans, only the first CE-T1WI showing BMs was used.

MRI preprocessing and segmentation

All CE-T1WI images were spatially normalized to the MNI152 template (Montreal Neurological Institute) [13, 17]. DICOM images were converted to NIfTI format using dcm2nii (University of Nottingham, UK). Registration was performed with SPM12 ('Normalize estimate and write' module) in MATLAB R2012a using default settings (Code S1). Hyperintense and ring-enhancing lesions were semi-automatically segmented with 3D Slicer (v4.10.0) to generate 3D ROIs [12, 18]. Manual delineation of lesion voxels was followed by automatic refinement via the 'Grow from Seed' tool. Three trained researchers (Z.D., J.W., Q.Y.) performed segmentation, which was independently validated by an experienced neurosurgeon (C.S.) and neuroradiologist (B.J.). The complete workflow is shown in **Figure 1b**.

Quantification of lesion characteristics

Centroid coordinates for each lesion were computed using custom MATLAB scripts (Code S2). Brain regions were defined as frontal, temporal, parietal, occipital, and insular lobes; limbic system (cingulate gyrus, hippocampus, parahippocampal gyrus, amygdala); thalamus and basal ganglia; cerebellum; and brainstem. The cerebellar vermis and brainstem were considered midline structures; remaining regions were divided into left and right hemispheres. Lesion locations were determined by mapping centroids to the corresponding brain areas (Code S2).

The number of lesions per patient and their volumes were calculated using MATLAB. Adjacent voxels were considered part of the same lesion if connected along any edge ('bwlabeln' function). Normalized lesion volume and brain region volume were derived by multiplying voxel counts by the single-voxel volume (0.08 mm^3).

Generation of tumor frequency and statistical heatmaps

After registering all ROIs to the MNI152 standard coordinate system, overlapping lesion maps were processed using MRIcron (University of Nottingham, UK) to generate three-dimensional tumor frequency heatmaps, illustrating the spatial distribution of BMs across the cohort **(Figure 1b)** [13].

To explore the association between lesion location and specific clinical characteristics, we constructed p-value heatmaps for comparative analysis of two distinct phenotypes (e.g., patients above vs. below the median age). Separate tumor frequency maps were first created for each phenotype. A 2 × 2 contingency table was then applied, and a two-tailed Fisher's exact test was performed to assess the significance of voxel-specific differences. This approach, known as analysis of differential involvement (ADIFFI), calculates the probability of observing the spatial distribution of lesions under the null hypothesis, as previously described by Ellingson and colleagues [15, 16].

$$p = \frac{(a+b)!\,(c+d)!\,(a+c)!\,(b+d)!}{a!\,b!\,c!\,d!\,n!} \quad (1)$$

This formula was used to calculate the significance of a particular voxel, where 'a' is the frequency of tumor occurrence under phenotype A, 'b' is the frequency of tumor occurrence under phenotype B, 'c' is the frequency of tumor-free patients under phenotype A, 'd' is the frequency of tumor-free patients under phenotype B, and 'n' is the total number of patients (Code S3 and S4).

Normalization of brain metastasis risk

To quantify the susceptibility of different brain regions to metastases independently of primary tumor type, we calculated the relative metastatic risk (RMR). The RMR for each region was adjusted based on the volume of that region, accounting for anatomical size differences and minimizing the bias introduced by unequal brain region volumes. This normalization allows for a more accurate comparison of metastatic likelihood across distinct anatomical areas.

$$\mathrm{RMR_X} = \frac{N_X/N_P/V_X}{\sum_{i=1}^{n=N_R}(N_i/N_P/V_i)/N_R} \quad (2)$$

N_x is the number of patients with BMs in a specific brain region. N_p is the sample size (1102 in our study). V_x is the volume of a specific brain region in MNI152, and N_R is the number of brain regions (18 in our study). After normalization, RMR_x represents the relative metastatic risk of BMs in the per unit volume of a specific brain region. $RMR_x > 1$ indicates BMs susceptibility. $RMR_x = 1$ indicates BMs neutrality, and $RMR_x < 1$ indicates BMs non-susceptibility.

Statistical analysis

Continuous variables are presented as mean ± standard error of the mean (SEM). Group comparisons were conducted using non-parametric methods, including the Mann-Whitney U test for two groups and the Kruskal-Wallis test for multiple groups. When post hoc pairwise comparisons were needed, Dunn's test was applied. Overall survival (OS) was defined as the interval from the first radiologically confirmed brain metastasis to either death or the last follow-up, with survival data available for 991 patients. Kaplan-Meier survival curves were generated to evaluate the association between clinical features and OS, with differences assessed via the log-rank test. To identify independent predictors of prognosis and adjust for confounding factors, multivariate Cox proportional hazards models were constructed. A threshold of $p < 0.05$ was considered statistically significant. All analyses were conducted using GraphPad Prism (v8.0.2, GraphPad Software, San Diego, CA) and IBM SPSS Statistics (v22.0, Armonk, NY, USA).

Conclusion

In summary, this study provides evidence that brain metastases located in the infratentorial regions are linked to certain clinical features and may indicate a less favorable prognosis. The application of voxel-wise mapping allowed for a detailed evaluation of BM distribution and its potential clinical relevance. These insights could enhance the precision of diagnostic assessments, guide therapeutic strategies, and improve prognostic predictions for patients with brain metastases.

Acknowledgments: None

Conflict of Interest: None

Financial Support: This research was funded by the Key Project of Ministry of Science and Technology of China (No. 2018YFA0108603 to C.S.) and the National Natural Science Foundation of China (No. 81771246 to G.C., No.81702462 to C.L., and No. 81870908 to F.Y.).

Ethics Statement: None

References

1. Villano JL, Durbin EB, Normandeau C, Thakkar JP, Moirangthem V, Davis FG. Incidence of brain metastasis at initial presentation of lung cancer. Neuro Oncol. 2015;17(1):122-8.
2. Ostrom QT, Wright CH, Barnholtz-Sloan JS. Brain metastases: Epidemiology. Handb Clin Neurol. 2018;149:27-42.
3. Doron H, Pukrop T, Erez N. A blazing landscape: Neuroinflammation shapes brain metastasis. Cancer Res. 2019;79(3):423-36.
4. Fabi A, Felici A, Metro G, Mirri A, Bria E, Telera S, et al. Brain metastases from solid tumors: Disease outcome according to type of treatment and therapeutic resources of the treating center. J Exp Clin Cancer Res. 2011;30(1):10.
5. Suh JH, Kotecha R, Chao ST, Ahluwalia MS, Sahgal A, Chang EL. Current approaches to the management of brain metastases. Nat Rev Clin Oncol. 2020;17(5):279-99.
6. Lo SS, Gore EM, Bradley JD, Buatti JM, Germano I, Ghafoori AP, et al. ACR Appropriateness Criteria® Pre-irradiation evaluation and management of brain metastases. J Palliat Med. 2014;17(8):880-6.
7. Cacho-Díaz B, Lorenzana-Mendoza NA, Chávez-Hernandez JD, González-Aguilar A, Reyes-Soto G, Herrera-Gómez Á. Clinical manifestations and location of brain metastases as prognostic markers. Curr Probl Cancer. 2019;43(5):312-23.
8. Emery A, Trifiletti DM, Romano KD, Patel N, Smolkin ME, Sheehan JP. More than just the number of brain metastases: Impact of location and relative volume on overall survival after stereotactic radiosurgery. World Neurosurg. 2017;99(1):111-7.
9. Akeret K, Staartjes VE, Vasella F, Serra C, Fierstra J, Neidert MC, et al. Distinct topographic-anatomical patterns in primary and secondary brain tumors and their therapeutic potential. J Neurooncol. 2020;149(1):73-85.
10. Bender ET, Tome WA. Distribution of brain metastases: Implications for non-uniform dose prescriptions. Br J Radiol. 2011;84(1001):649-58.
11. Mampre D, Ehresman J, Alvarado-Estrada K, Wijesekera O, Sarabia-Estrada R, Quinones-Hinojosa A, et al. Propensity for different vascular distributions and cerebral edema of intraparenchymal brain metastases. J Neurooncol. 2019;143(1):115-22.
12. Quattrocchi CC, Errante Y, Gaudino C, Mallio CA, Giona A, Santini D, et al. Spatial brain distribution of intra-axial metastatic lesions in breast and lung cancer patients. J Neurooncol. 2012;110(1):79-87.
13. Takano K, Kinoshita M, Takagaki M, Sakai M, Tateishi S, Achiha T, et al. Different spatial distributions of brain metastases from lung cancer by histological subtype and EGFR mutation. Neuro Oncol. 2016;18(5):716-24.
14. Kyeong S, Cha YJ, Ahn SG, Suh SH, Son EJ, Ahn SJ. Subtypes of breast cancer show different spatial distributions of brain metastases. PLoS One. 2017;12(11):e0188542.
15. Ellingson BM, Cloughesy TF, Pope WB, Zaw TM, Phillips H, Lalezari S, et al. Anatomic localization of MGMT-methylated and unmethylated tumors: Radiographic study in 358 de novo glioblastomas. Neuroimage. 2012;59(1):908-16.
16. Ellingson BM, Lai A, Harris RJ, Selfridge JM, Yong WH, Das K, et al. Probabilistic radiographic atlas of glioblastoma phenotypes. AJNR Am J Neuroradiol. 2013;34(3):533-40.
17. Yamashita K, Hiwatashi A, Togao O, Kikuchi K, Momosaka D, Hata N, et al. Differences between primary central nervous system lymphoma and glioblastoma: Topographic analysis using voxel-based morphometry. Clin Radiol. 2019;74(10):816.e1–8.
18. Fedorov A, Beichel R, Kalpathy-Cramer J, Finet J, Fillion-Robin JC, Pujol S, et al. 3D Slicer as an image computing platform for the Quantitative Imaging Network. Magn Reson Imaging. 2012;30(9):1323–41.